On the pronounced mode dependency of the interface fracture toughness of pressureless sintered silver interconnects

Identification of dissipative micro-mechanisms

Schoenmakers, Noud P.T.; Hoefnagels, Johan P.M.; Smits, Edsger C.P.; van der Sluis, Olaf

DOI
10.1016/j.engfracmech.2025.110860

Publication date
2025

Document Version
Final published version

Published in
Engineering Fracture Mechanics

Citation (APA)
Schoenmakers, N. P. T., Hoefnagels, J. P. M., Smits, E. C. P., & van der Sluis, O. (2025). On the pronounced mode dependency of the interface fracture toughness of pressureless sintered silver interconnects: Identification of dissipative micro-mechanisms. *Engineering Fracture Mechanics*, *316*, Article 110860. https://doi.org/10.1016/j.engfracmech.2025.110860

Engineering Fracture Mechanics 316 (2025) 110860

Contents lists available at ScienceDirect

Engineering Fracture Mechanics

journal homepage: www.elsevier.com/locate/engfracmech

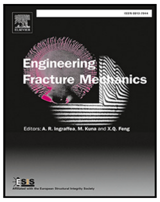

On the pronounced mode dependency of the interface fracture toughness of pressureless sintered silver interconnects: Identification of dissipative micro-mechanisms

Noud P.T. Schoenmakers [a,b,c], Johan P.M. Hoefnagels [a], Edsger C.P. Smits [b], Olaf van der Sluis [a,*]

[a] *Eindhoven University of Technology, Eindhoven, The Netherlands*
[b] *Chip Integration Technology Center, Nijmegen, The Netherlands*
[c] *Delft University of Technology, Delft, The Netherlands*

ARTICLE INFO

Keywords:
Interface fracture toughness
Mode mixity
Sintered silver
Adhesion
Delamination
Microstructure

ABSTRACT

The microscopic failure mechanisms contributing to the interface fracture toughness of two different pressureless sintered silver interconnects during mixed-mode delamination tests have been studied. Two sintered silver materials are used, one containing nanoparticles (NP) and one containing microflakes (μF). The adhesives are sintered between two 35 × 5 mm^2 copper plates electroplated with a silver backside metallisation layer. The fracture behaviour has been monitored under in-situ optical microscopy using the miniature mixed-mode bending setup, combined with post-mortem Scanning Electron Microscopy (SEM) fractography analysis. The significant difference in microstructure between the two interconnect materials results in a pronounced difference in failure behaviour, and resulting mixed-mode interface fracture toughness. The two main competing failure mechanisms are interface delamination and bulk fracture. The NP-interconnect exhibits the typical increase in interface fracture toughness with increasing mode angle, whilst the μF-interconnect shows a never reported before dependency, having a global minimum. The fracture morphologies of the delaminated samples are analysed to explain the difference in failure behaviour using Scanning Electron Microscope (SEM) images. This study offers valuable insights into the complex interplay between the microstructures of the interconnect, failure mechanisms, and the resulting interface fracture toughness.

1. Introduction

For decades, lead-holding solders have been used successfully as package interconnect material in power electronics, e.g., Tummala et al. [1]. However, European legislation, specifically the End-of-Life Vehicle (ELV) directive 2000/53/CE [2] and the Restriction of Hazardous Substances (RoHS) [3], restricts the use of certain hazardous substances (i.e. lead, mercury, hexavalent chromium, and cadmium). For die-attached interconnect materials in particular, an appropriate alternative has yet to be found; hence, the RoHS has extended the exception for the use of lead-holding solders up until 2026, and the ELV directive exemption from 2024 onwards is still under review by the time of writing [4,5]. The challenge is to find an alternative that can dissipate the accumulated heat and cyclic thermal expansion while ensuring mechanical reliability and electrical connectivity.

---

[*] Corresponding author.
E-mail address: o.v.d.sluis@tue.nl (O. van der Sluis).

https://doi.org/10.1016/j.engfracmech.2025.110860
Received 11 October 2024; Received in revised form 21 January 2025; Accepted 25 January 2025

Nomenclature

Γ	Fracture toughness
γ	Characteristic dimension of the MMMB
μF	Micro flake
ψ	Mode angle
BSM	Back Side Metallisation
DIC	Digital Image Correlation
ELV	End-of-Life
FIB	Focused Ion Beam
IF	Interface
MMMB	Miniature Mixed Mode Bending
RoHS	Restriction of Hazardous Substances
SEM	Scanning Electron Microscope
WoS	Work of Separation
ξ	Dimensionless shape parameter
A	Area
a	Crack length
B	Out-of-plane sample thickness
F	Force
H	Absolute position of the mode selector
K	Stress intensity factor
t	In plane thickness
U	Energy
v	Displacement
W	Sample length
NP	Nanoparticle

Already in 1997, sintered interconnects have been recognised as a very promising alternative to the above-mentioned solder materials [6]. Here, micro- and nano-sized particles sinter, with or without pressure assistance, to a dense but porous microstructure with the same melting temperate as its bulk structure [7,8]. For high-power semiconductor devices, silver- and copper-based sinters are the most promising candidates [4,9]. Due to their excellent thermal conductivity ($100-400$ [W/mK]), high melting temperature (961 [°C]), acceptable shear strength ($20-80$ [MPa]), and low processing temperature (as low as 150 [°C]), sintered silver materials are of particular importance [10–20]. Note that the required sintering temperature depends on the initial particle shapes and sizes, the use of additives, and the amount of pressure applied during sintering.

Evidently, to efficiently process sintered materials with desired properties, it is crucial to establish the correlation between the microstructure of the material after sintering and the resulting relevant material properties at (macroscopic) product level. For example, Ordonez Miranda et al. [21] quantified the thermal conductivity from measurements and models. Gillman et al. [22] established the elastic and thermal properties directly from the microstructural statistics obtained from Focused Ion Beam (FIB) milling combined with Scanning Electron Microscope (SEM) images, and computational homogenisation, assuming the macroscopic mechanical and thermal properties for the intrinsic material behaviour of the silver particles. Chen et al. [23] studied the temperature-dependent fracture behaviour in tension and shear through flat tensile specimens and die shear tests. More recently, it became clear through die shear testing that the sintered silver-copper interface can be prone to failure [20].

Interconnect bonding properties have been experimentally characterised. For example, Lee and Yoon [24] compared the shear strength of sintered silver with Cu, Ag and electroless-nickel-immersion gold surface finishes. It could be concluded that Ag surface finish outperforms Cu and Au surface finishes, which was confirmed by Zhao et al. [25] and Wang et al. [26], where shearing fracture toughness was measured as a function of sintering temperature and surface finishes (in this case, Cu, Ni, Au and Ag). Dai et al. [27] studied the effect of micropatterning of the copper substrate on interface fracture toughness under mode II conditions in the end notch flexure test. It was concluded that certain pattern geometries trigger the transition from interface to bulk fracture, which enhances interface fracture toughness. This interface crack deflection mechanism has also been observed in copper–epoxy moulding compound interfaces [28].

Almost all studies focus on the mode II fracture toughness of sintered silver interconnects [20,25,27,29–33]. Although it is logical to look into these values due to the high shear stresses that occur around the sides of the die, this study will show that the entire range of mode mixities is important for sintered silver interconnects, as it appears to be more complex than initially imagined.

Therefore, to elaborate on our understanding of the relevant dissipative mechanisms around the sintered silver–silver backside metallisation (Ag-BSM) interface and the sintered silver bulk, mixed-mode interface delamination experiments will be performed. In particular, the Miniature Mixed-Mode Bending (MMMB) setup, as developed by Kolluri et al. [34,35], will be applied to quantify the interface fracture data in the full range of mode mixities. By capturing the delamination process *in situ* under an optical microscope, the fracture toughness for each mode angle is determined by the change in crack length, accurately obtained through digital image correlation (DIC), and the measured force–displacement curve. In this paper, mixed mode fracture toughness data are obtained for two distinct sintered silver materials: one containing nanoparticles (NP) and one mainly containing microflakes (μF). All samples are sintered without pressure at 250 [°C] and 280 [°C]. Pressure sintering is not preferred for high-volume production in the power packaging industry. The specific mode angles are determined through numerical simulations of the fracture process. After delamination, the morphology of the fracture surfaces is investigated using a Scanning Electron Microscope (SEM) and an optical microscope. In addition, the sintered microstructure is investigated using an SEM, after polishing and ion beam milling. Similar to the work of Neggers et al. [36], this work distinguishes three scales: macro, meso and micro. At the macroscopic scale (i.e., the product or sample scale) the load is applied. Consequently, the experimentally measured fracture toughness corresponds to the interface fracture toughness value, also reported as work of separation (WoS). The mesoscopic scale is defined by the fracture process zone. At this scale, the interconnect material is considered a uniform, homogenised material and the mode angle is calculated. The dissipative mechanisms are active at the microscopic scale. Here, the material is heterogeneous due to the discreteness of the microstructure. At this scale, the dissipative failure mechanisms are identified, such as cohesive and adhesive failure. As a result, the effect of these different mechanisms on the macroscopic interface fracture toughness is quantified.

2. Experimental methods

Miniature mixed mode bending setup

To accurately characterise the interface fracture toughness of sintered silver interconnects as function of mode angle in multilayer samples having representative dimensions for microelectronics applications, the Miniature Mixed Mode Bending Device (MMMB) is used, which was specifically developed by Kolluri et al. [34,35] for high-resolution investigation of delamination and fracture in microelectronic components. The device is schematically shown in Fig. 1. It allows for *in situ* characterisation of interface fracture toughness over the full range of mode mixities at a constant mode angle during each test. Changing the mode selector (2) affects the ratio of forces F_A and F_B, and thus the mode angle. In particular, the position at which $\xi = H/\gamma = 0$ results in (far-field) mode I loading, that is, $\psi = 0°$, while $\xi = 1$ corresponds to (far-field) end notch flexure test, i.e., $\psi = 90°$. Evidently, intermediate mode angles are obtained by the positions $0 < \xi < 1$. The width of the setup is 36.5 [mm], while the sample dimensions are as follows: length $W = 35.0$ [mm], width (in the out-of-plane direction of the setup) $B = 5.0$ [mm], copper layer thickness $t_{\mathrm{Cu}} = 0.5$ [mm], silver backside metallisation layer $t_{BSM} \approx 5$ [μm], sintered silver interconnect thickness $t_{\mathrm{Ags}} \approx 40$ [μm], and pre-crack length $a_0 = 5$ [mm]. The setup is mounted in an *in situ* micro-tensile stage. Details on the MMMB setup can be found in the dedicated publications of Kolluri et al. [34,35,37]. Note that the device has been carefully designed to minimise energy dissipation in the setup using optimised elastic hinges and so-called dovetail connectors to take out all play from the system.

Sample manufacturing and preparation

Samples are made from two strips of leadframe grade C194 copper plates, electroplated with a silver backside metallisation layer (BSM) and sintered together using Ag sinter. First, a large 0.5 [mm]-thick plate of copper is chemically cleaned and activated, after which the 5 [µm]-thick BSM layer is applied by electroplating. Next, 35 × 5 [mm^2] copper-BSM strips are cut out, using laser cutting, and placed in a dedicated milled aluminium holder, and Kapton tape is applied over the last 5 [mm] of strip length to later create the 5 [mm]-long (blunt) pre-crack. Subsequently, the strips are covered with a dedicated stencil device and silver paste is applied and evenly distributed over the surface using a Japanese putty knife. The stencil and tape are then removed. To create the 5-layer sample structure, a second copper-BSM strip is precisely placed on top of the first strip, upside down, guided by a second milled aluminium holder. The samples are then put in a sintering oven. To prevent the oxidation of silver during the curing and the sintering phases, N2 gas flows through the chamber. The thus created blunt pre-crack is shown in Fig. 1d. The pre-crack length varies with ±0.5 [mm], which results in acceptable reproducibility, as the first loading cycle is omitted from the toughness analysis in any case, as explained below. After sintering, the side of the 5-layer samples are sanded to remove excess sintered silver.

To accurately quantify the displacement field during mixed-mode bending, digital image correlation (DIC) is used at a magnification of 12x corresponding to a pixel size of ≈ 7 [μm/px]. For this purpose, a speckle pattern is applied by spraying conductive black paint off-axially through a tube, resulting in a dense, random speckle pattern. After applying the DIC pattern with speckles between 6 and 10 pixels, the dovetails are glued onto the sample after which the sample is mounted into the MMMB setup. It is important to note that the added speckle pattern is extremely thin compared to the 5 [mm] thick copper sample and does not affect the fracture toughness results.

Initialisation of measurements

Prior to starting the experiment, a stereo microscope (ZEISS steREO Discovery.V20) with an Axiocam 506 mono camera, with 2752 × 2208 pixels, is focused on the applied speckle pattern on the sample and positioned so that the centre loading anvil (corresponding to F_B in Fig. 1) and the dovetails are in the microscope field of view, of which an example is provided in Fig. 2.

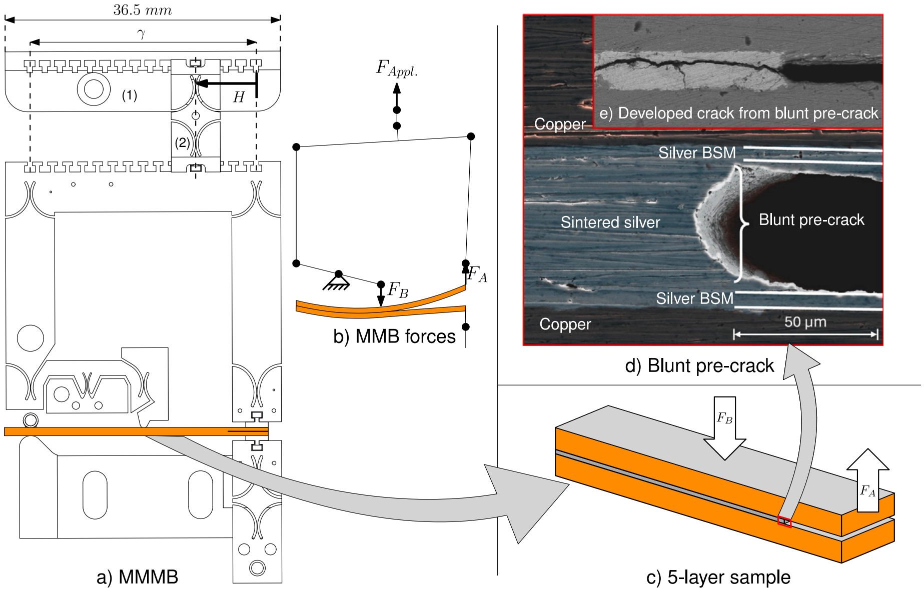

Fig. 1. (a) Schematic illustration of the MMMB setup developed by Kolluri et al. [34,35], with (1) the position selector, (2) the mode selector with dovetail hinges, and the 5-layer sample in orange; (b) a schematic representation of the workings of the MMMB setup; (c) Cu/Ag/Cu material sample geometry; (d) SEM image of the created blunt pre-crack. From top to centre: the copper plate, the backside metallisation layer, and the sintered silver layer. The surface roughness is exaggerated in the SEM picture, as the BSE layer was smeared out due to a relatively rough sanding process to retain the blunt pre-crack shape ; (e) example of a propagated sharp crack initiated from the blunt pre-crack.

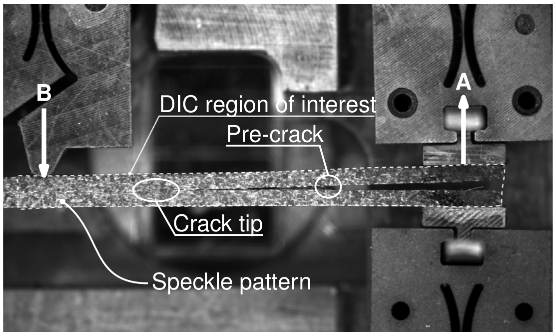

Fig. 2. Example of a mode I delamination experiment (i.e., $\xi = 0$) in the MMMB setup, where the interface crack propagates from right to left. Observe the speckle pattern applied to the sample. DIC is performed on the region of interest indicated by the dashed line.

Measuring and processing

Multiple loading – interface crack propagation – unloading cycles are conducted until the crack tip approaches the centre loading anvil. To calculate the fracture toughness for each mode angle, the resulting force–displacement curve is used. The fracture toughness is calculated by Gdoutos [38]:

$$\Gamma_{C,i}(\psi) = -\frac{1}{B}\frac{\Delta U_i}{\Delta a_i} \tag{1}$$

where B is the out-of-plane sample thickness, ΔU_i the area that represents the dissipated energy between the loading and unloading lines for the different crack lengths Δa_i, and $\Delta a_i = a_{i+1} - a_i$ the change in crack length between the subsequent loading–unloading curves, as shown in Fig. 3. For each mode angle a new experiment is performed. Multiple data points are obtained for each test, as multiple loading – crack propagation – unloading cycles are performed. Note that fracture toughness is calculated during steady-state crack propagation with a fully developed fracture process zone. Consequently, the initial loading cycle is omitted from the analysis because this is when the steady-state fracture process zone evolves from the introduced pre-crack. The curves clearly show irreversible plastic deformation, most likely occurring in the sintered silver layer. As a result, the calculated Γ_C values correspond to the so-called macroscopic work of separation, which includes the energy dissipation caused by plasticity. As the scope of this manuscript is to identify the dissipative mechanisms around the interface, it is not required to separate the individual energy contributions to the macroscopic interface fracture toughness. It is remarked that a combined numerical–experimental approach

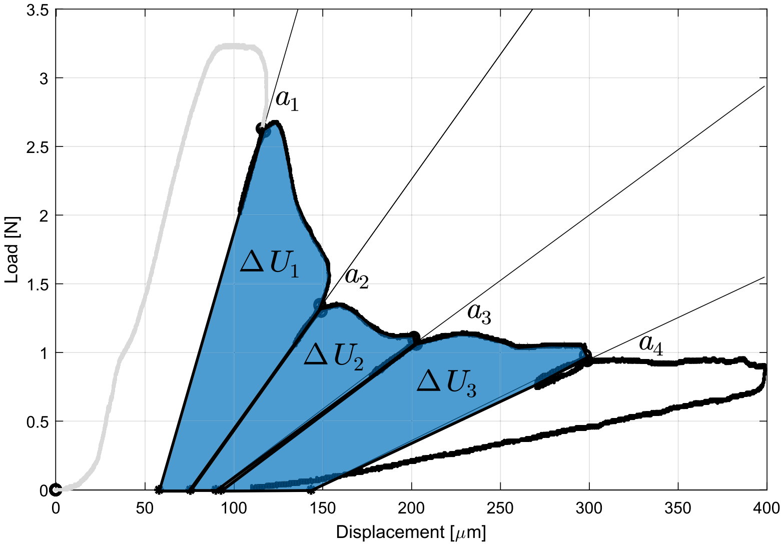

Fig. 3. The areas that represent the dissipated energies ΔU_i due to fracture between the subsequent loading and unloading lines a_i and a_{i+1}. The curve's initial segment, where crack initiation occurs, is shaded in grey.

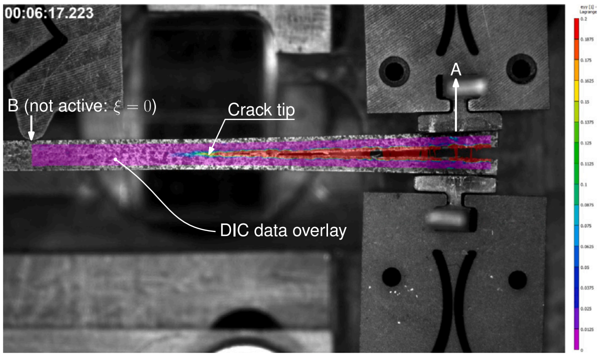

Fig. 4. The ε_{yy} DIC strain component field shown as an overlay on the delaminated sample. The full video can be found on: https://youtu.be/xXvyQqueStc. Note that the example experiment shown here is a mode I experiment, where the mode selector is placed all the way to the right ($\xi = 0$). Hence, as indicated, no forces are acting through point B, only through point A.

could be employed for the identification of the individual contributions (see, e.g., Kolluri et al. [39]).

In order to obtain the energy as the integral of the force over the displacement, as shown in Fig. 3, this displacement needs to be obtained at the position of the load cell, which could be measured by the LVDT that measures the applied displacement at the clamps, $v_{appl.}$. However, it was found to be more accurate to determine $v_{appl.}$ from the displacement measured by DIC at anvil A and B and converting those to $v_{appl.}$ using the kinematic equation of the MMMB elastic mechanism, as obtained by Samimi et al. [40],

$$v_{appl.} = v_A(1-\xi) - \xi v_B, \tag{2}$$

where $v_{appl.}$ is the displacement without the elastic deformation of the MMMB, and v_A, and v_B are the displacements measured using DIC. The change in crack length is also determined through DIC. The crack tip is tracked using the strain field peak obtained around the centre of the sample, between the two individual plates. A snapshot example of the obtained DIC strain field is shown in Fig. 4.

To establish the relation between the mode angle ψ and the dimensionless shape parameter ξ, 2D finite element simulations at mesoscopic level of the full specimen geometry including the silver BSM layers and the two C194 copper plates are performed in MSC.Marc. The model consists of a focused crack tip mesh with collapsed quadratic quarter point elements to accurately describe the stress singularity at the crack tip [41–43], and is shown in Fig. 5. Due to the out-of-plane thickness of 5 [mm], plane strain is assumed and frictionless contact is prescribed between the different materials to avoid material penetration. By varying ξ and maintaining a constant applied force F, the forces F_A and F_B are given by $F_A = F \cdot (1-\xi)$ and $F_B = F \cdot \xi$. The mode angle is determined by the ratio of the interface stress intensity factors K_1 and K_2: $\psi = \tan^{-1}\left(\frac{K_2}{K_1}\right)$. The interface stress intensity factors are determined through the interaction integral method [44–46]. The interaction integral method is validated through an extrapolation method in which the

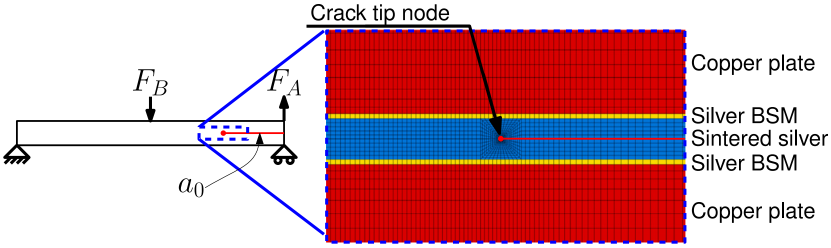

Fig. 5. The focused crack tip mesh used for the FE simulation to determine the SIFs for each ξ. The crack tip node is located in the centre, while the red line shows the pre-crack a_0.

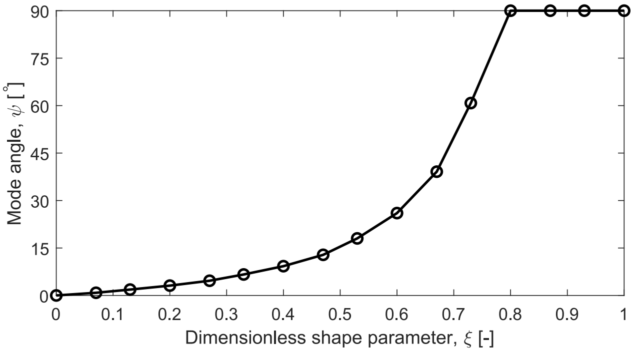

Fig. 6. The dimensionless shape parameter ξ versus the mode angle ψ as calculated from the finite element simulations.

stress intensity factors are calculated from the crack tip opening displacements at different r values and subsequently extrapolated to $r = 0$, where r is the distance from the crack tip node [47,48]. The result is shown in Fig. 6. Mesh independency is checked by refining the mesh with a factor of 10 in both directions; the difference in the calculated mode angle is 0.03%, which indicates a converged result. Note that pure mode II is obtained at $\xi \simeq 0.8$, similar to Kolluri et al. [37], while for higher ξ an additional compressive stress normal to the process zone exists, which increases with increasing ξ until the end-notch flexure (ENF) configuration is reached at $\xi = 1$. This is an important distinction of the MMMB setup compared to a regular ENF setup, as the sintered interconnects are porous, thus creating friction along the cracked interface, which would increase the measured force response and the corresponding fracture toughness.

Fracture surface morphology analysis

After testing, the samples are carefully cleaned using cotton swabs with alcohol to remove the DIC speckle pattern, while preserving the crack. The samples are analysed in a FEI Quanta 600 SEM using the backscatter electron (BSE) mode to identify the complex crack propagation path. In addition, the separated fracture surfaces are studied under a Zeiss V20 optical microscope to identify regions of interface and bulk fracture through the greyscale levels of the obtained images. As illustrated in Fig. 7, the fracture surfaces have a specific reflection. The bulk fracture is seen as much darker, whilst the interface fracture appears lighter. The two sides of the interface fracture can be distinguished, see Fig. 7, as surface (3) reflects more of the silver backside metallisation layer, therefore reflecting much whiter than surface (2). The relative area of these three surfaces is calculated from the peaks fitted to the combined histogram image, as shown in Fig. 7.c, using the open source Matlab peak fitting toolbox provided by O'Haver [49]. Using the relative areas, the percentage of bulk failure is determined through Bulk% $= \frac{A_1}{A_{total}}$ and the percentage of interface failure through IF% $= \frac{2*\min(A_2,A_3)}{A_{total}}$.

3. Experimental results

Two sintered silver interconnect materials are considered in this study: one material is composed of nanoparticles (NP) while the second material is mainly composed of microflakes (μF). Fig. 8 shows SEM images of typical microstructures of both unsintered materials, from which the particle size difference is clearly visible. The particle size of the NP material ranges from 100 [nm] to 800 [nm], whereas the particle size of the μF material ranges from 3 [μm] to 10 [μm]. The resulting microstructures after sintering at two different temperatures are shown in Fig. 9, together with an estimation of the porosity, obtained by converting the greyscale BSE images to a binary value. Specific observations for the different materials are discussed in the corresponding sections below.

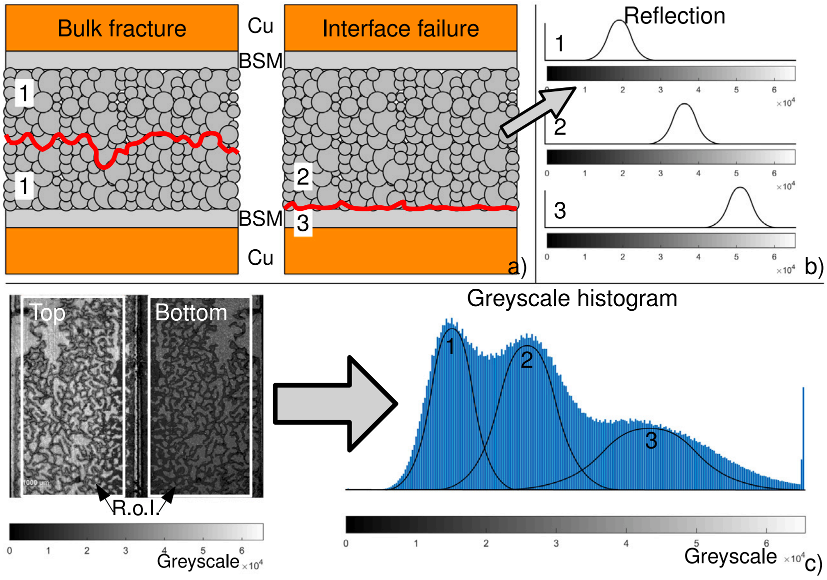

Fig. 7. The process of determining the fracture morphology per sample, where a) represents a schematic cross-section of the fractured surface, b) the greyscale distribution when visualising the three variants of fractured surfaces, and c) a measurement of the top and bottom of a fractured sample under a stereo light microscope and the corresponding histogram together with the equations used to determine the area percentage of bulk fracture versus interface fracture.

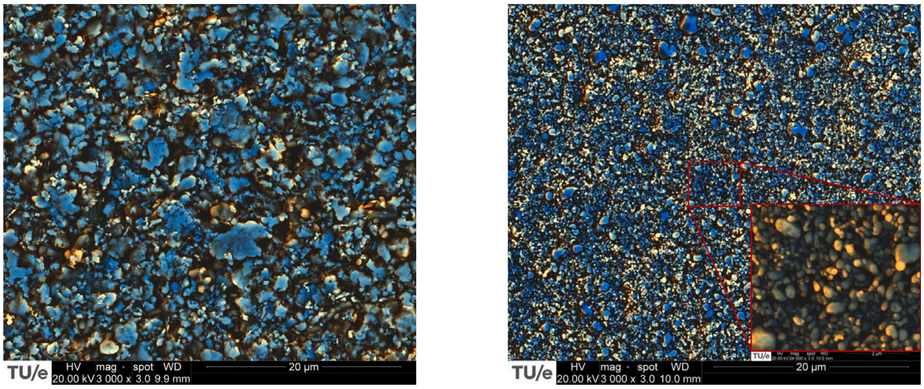

(a)

(b)

Fig. 8. SEM images of the microstructures of unsintered silver cured by evaporating the solvents under high vacuum for approximately 2 h to enable SEM observation, (a) microflakes and (b) nanoparticles, with a factor 10 increased magnification to show the individual particles.

3.1. Nanoparticle sintered silver

From Fig. 9a,c, it can be observed that increasing the temperature increases the homogeneity of the microstructure of the nanoparticle material. At 250 [°C], more small islands are visible, whereas these islands almost completely disappear at 280 [°C]. This can be explained by the fact that at lower temperatures, the smallest nanoparticles agglomerate whilst the activation energy for agglomeration of the larger nanoparticles is not yet reached, therefore, at a higher sintering temperature particles tend to agglomerate faster, forming a more homogeneous small-scale microstructure, and thereby also decreasing the porosity. The diffusion coefficient obeys an Arrhenius equation resulting in higher diffusion values at higher temperatures [7,50]. This aligns with the observation of reduced porosity with increasing sinter temperature, as shown by Knoer and Schletz [51] for pressureless sintered silver nanoparticles.

The measured interface fracture toughness, or work of separation (WoS), values as a function of the mode angle, for the two sintering temperatures, are shown in Fig. 10. As illustrated by the linear fits, the work of separation shows an approximately linear dependency with the mode angle. This is somewhat uncharacteristic, as typical mixed-mode interface fracture data exhibit a highly nonlinear relation with the WoS sharply increasing towards mode II loading [37,52,53].

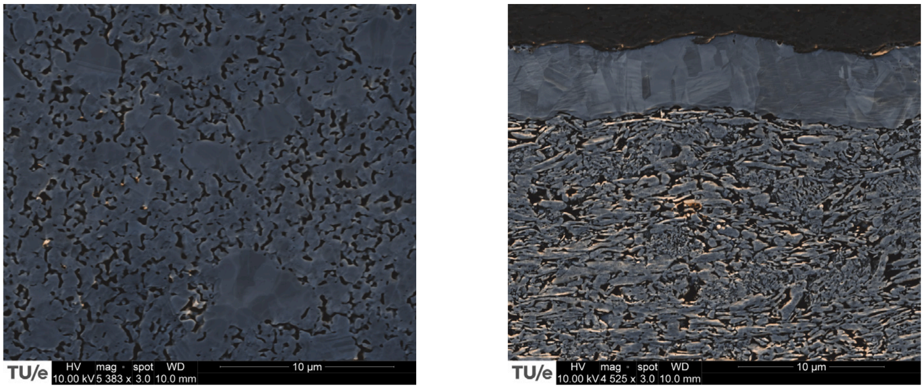

(a) The nanoparticle material, T_{sinter} = 250 [°C], porosity ≈ 19%

(b) The microflake material, T_{sinter} = 250 [°C], porosity ≈ 30%

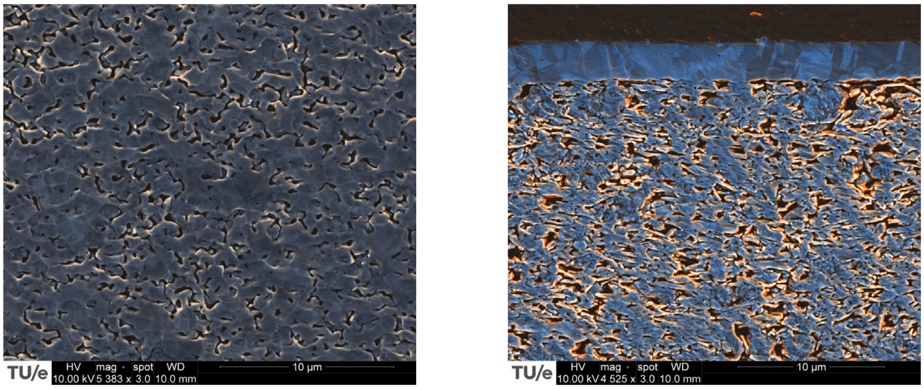

(c) The nanoparticle material, T_{sinter} = 280 [°C], porosity ≈ 14%

(d) The microflake material, T_{sinter} = 280 [°C], porosity ≈ 26%

Fig. 9. SEM images of the microstructures of the (a,c) nanoparticle, and (b,d) microflake materials, sintered at two different temperatures. The SEM images consist of a combination of SE and BSE, the bright hotspots are a result of brightness-contrast settings.

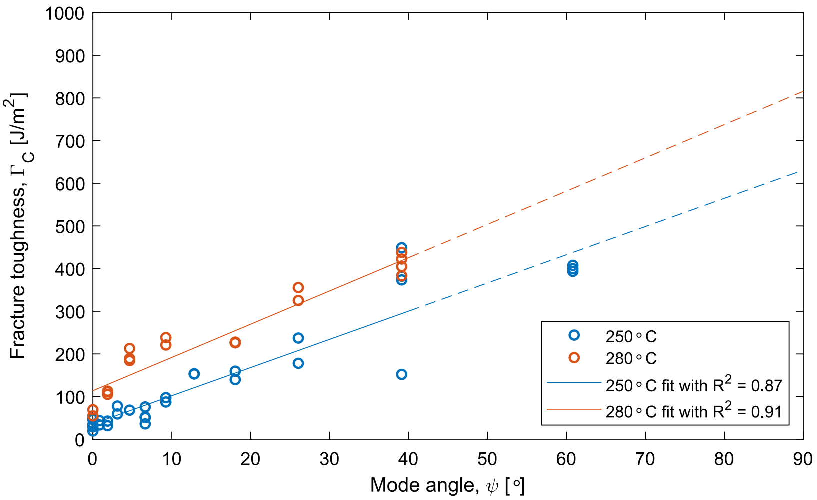

Fig. 10. Interface fracture toughness of the nanoparticle sintered silver as a function of mode angle and sintering temperature. A linear fit was used for both temperatures, which gives reasonable R^2 values.

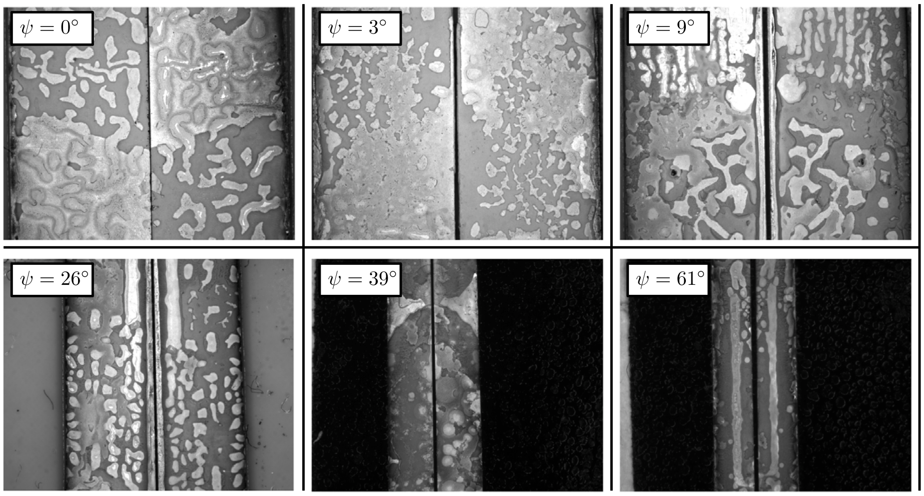

Fig. 11. Stereo light microscopy images of the top and bottom fracture surfaces of the delaminated nanoparticle sintered silver samples.

Due to the maximum force level of the MMMB, performing a pure mode II test was impossible. The sample width was already reduced to $1.8 \leq B < 5$ [mm] for the higher mode angle tests, e.g. $\psi > 39°$, but the maximum force is still reached for the pure mode II test. Further reduction in the sample width was not possible as it resulted in contact between the hinges, which compromised the integrity of the experimental setup.

It can be concluded that a higher sintering temperature results in a higher work of separation which can be attributed to the more uniform microstructure of the sintered material. Moreover, the increasing fracture toughness as a function of the mode angle can be attributed to the increased plastic deformation at, and in front of, the crack tip, as there is no change in the fracture morphology of the specimens; see Fig. 11.

3.2. Microflake sintered silver

The resulting microstructures of the sintered silver containing microflakes, shown in Fig. 9b,d. It can be seen that both microstructures have regions of fine particles amidst a “matrix” of larger, highly elongated particles, i.e. microflakes, a few micrometres in size. Interestingly, these regions with fine particles are clearly more bonded for the 280 [$°C$] case, while for the 250 [$°C$] case many of these fine particles are loosely bonded. In contrast, no clear distinction can be observed in the degree of bonding of the microflakes. The measured interface fracture toughness values as a function of the mode angle and the two sintering temperatures are shown in Fig. 12. Several interesting observations can be made. Firstly, an atypical dependency of the fracture toughness on mode angle is observed: a decrease in fracture toughness occurs at small mode angles, i.e., $\psi < 10°$. For $10° < \psi < 20°$, Γ_C does not change significantly, while showing a minimum value. Subsequently, for $20° < \psi < 40°$, the fracture toughness increases, suggesting an additional, or different, mode angle-dependent dissipative mechanism for $\psi > 20°$, which is also atypical. For $\psi > 40°$, the fracture toughness remains constant, which is also atypical as a sharp rise towards mode II was expected as discussed above. Secondly, the fracture toughness values are at least one order of magnitude smaller than the values for nanoparticle-based sintered silver, indicating a large change in the failure mechanism compared to those for nanoparticle-based sintered silver. Finally, the interface fracture toughness does not show a clear dependency on the sintering temperatures, which is in contrast to that of nanoparticle-based sintered silver. This can be explained by the above-mentioned fact that a clear difference in the sintered microstructure is not observed for the two sintering temperatures and the lack of change in the failure mechanism with increasing sintering temperature. This seems to suggest that the fracture occurs along the bonding between the microflakes, avoiding regions with fine particles because a clear temperature dependence was found in the fine particles, but not for the matrix of microflakes. This suggests that the regions of fine particles have a higher WoS, which may explain the factor of 10 higher WoS of the nanoparticle sintered silver, as this consists completely of finer particles.

For this material, it was possible to perform pure mode II due to the significantly lower adhesion, it is possible in terms of maximum force and hinge range, even without altering the width of the specimen. However, stable crack growth could not be reached. The explanation for this is that during the first part of the test, the fracture process zone (almost) reaches the centre anvil, which is a well-known problem for mode II experiments using a three-point bending test [54]. This was concluded as the resulting force–displacement curve increased after the crack was initiated, indicating that the centre loading anvil interfered with the fracture, effectively withholding it from propagating.

To explain the peculiar mixed-mode behaviour, the fracture morphology will be analysed in more detail.

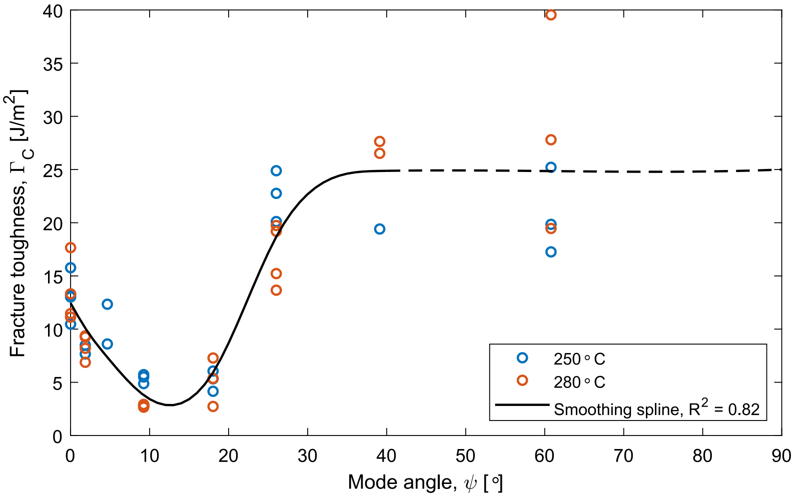

Fig. 12. Interface fracture toughness of the microflake sintered silver as a function of mode angle and sintering temperature. A smoothing spline fit was used for the combination of both temperatures, which gives reasonable R^2 values and stresses the atypical behaviour of the fracture toughness across the mode mixity.

Analysis of fracture morphology

From the SEM pictures in Fig. 13, two fracture morphologies can be distinguished clearly: (1) bulk (cohesive) fracture in the sintered silver material, (2) interface (adhesive) fracture at the interface between the sintered silver material and the BSM layers. Specifically, for tests conducted at $\psi = 9°$ and $\psi = 18°$, a pronounced preference for interface failure between the BSM and sintered silver layers is observed. In these cases, the bulk fracture represented less than 10% of the crack surface. A combined bulk-interface fracture pattern is visible and is referred to as interface crack deflection. The remaining mode angles, e.g. $\psi = 0°$, 2°, 26°, and 39° exhibit predominantly bulk fracture and $\psi = 61°$ a combination of both.

The occurrence of bulk and interface fracture is confirmed by stereo light microscope images of the top and bottom fracture surfaces for the various mode angles, see Fig. 14. Here, the brighter grey on the top or bottom side of the fracture surface corresponds to the BSM material which indicates interface failure, occurring mainly in $\psi = 9°$ and $\psi = 18°$. In contrast, a darker grey at the top and bottom sides of the fracture surface indicates bulk failure in the sintered silver material.

Consequently, Fig. 15 provides a quantitative calculation of the percentage of fracture morphology type as a function of the mode angle. What can be seen from the quantitative calculation is that the dip in fracture toughness at $0° < \psi < 30°$ corresponds to the peak in interface failure morphology of up to 70% at a mode angle of 9°. This calculation also showed more interface fracture than previously expected from the SEM BSE side view images at 0°, 2°, and 18°. For the higher mode angles of $\psi > 26°$, while some areas are inconclusive, there does not appear to be any indication of the presence of interface fracture of more than 10%.

Using the data presented in Fig. 15, an interesting observation can be made. Upon plotting the fracture toughness versus the relative amount of interface failure, the fracture toughness at 100% interface failure can be estimated. This is presented in Fig. 16. The best possible fit seems to be an exponential model. Given that the interface fracture toughness is equal to the thermodynamic work of adhesion Γ_0 and the micro- and macro-scale dissipative mechanisms Γ_D [43,53] through

$$\Gamma_C = \Gamma_0 + \Gamma_D, \tag{3}$$

it is possible to estimate the thermodynamic work of adhesion between the silver backside metallisation layer and the sintered silver. This estimate is illustrated in Fig. 16, yielding $\Gamma_0 \approx 1.7$ [J/m^2] which appears to be a reasonable value. Interestingly, the exponential fit in Fig. 16 would also mean that Γ_D increases with decreasing interface fracture, which may indicate that a crack front that partially runs over the interface restricts the bulk part of the fracture, thus limiting the extent to which dissipative mechanisms can be activated in the bulk. For full bulk fracture, the crack front fully activates all dissipative mechanisms resulting in a work of separation of $\Gamma_D \approx 25$ [J/m^2] for the microflake-based sintered silver material.

3.3. Comparison to literature

The obtained fracture toughness values are compared to values reported in the literature. Table 1 presents an overview of these values, including the test method used, porosity, and failure type for fracture mode I and mode II. Mode I toughness values range from 0.08 [J/m^2] in 3-point chevron tests to 70.1 [J/m^2] in double cantilever beam (DCB) tests of sintered silver reinforced with nickel-coated multiwall carbon nanotube (NiC tube) with a porosity of 25%. In mode II, toughness values range between 5–330 [J/m^2] in end-notch flexure (ENF) tests with porosities of 34–24%, and 277–969 [J/m^2] in Ag-BSM-reinforced sintered silver with porosities of 30 ± 3–25 ± 2%, also tested with ENF.

For nanoparticle-based sintered silver with 19–24% porosity measured in this work, $\Gamma_{I,C}$ values of 35–115 [J/m^2] and $\Gamma_{II,C}$ values of approximately 600–800 [J/m^2] are achieved. The results of Zhao et al. [25] suggest that these values fall within an acceptable

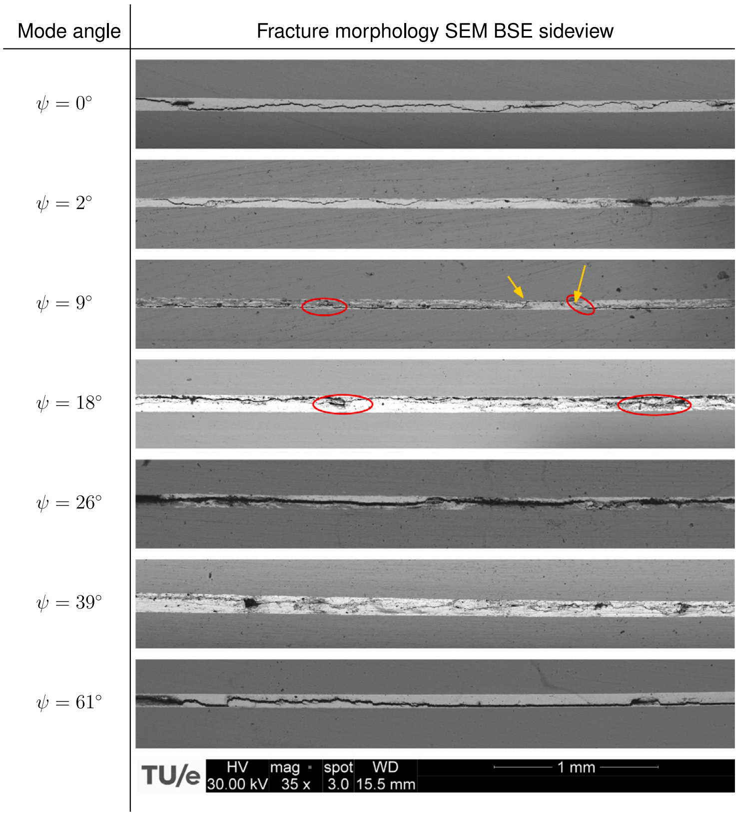

Fig. 13. The SEM BSE side view images of the samples after delamination as a function of mode angle $T = 280$ [$°C$] for the microflake sintered silver. At most mode angles, bulk fracture occurs primarily. However, at $\psi = 9°$ and $\psi = 18°$ mostly interface fracture between the sintered silver and the BSM layers occurs. At $\psi = 61°$, combined bulk and interface fracture occurs.

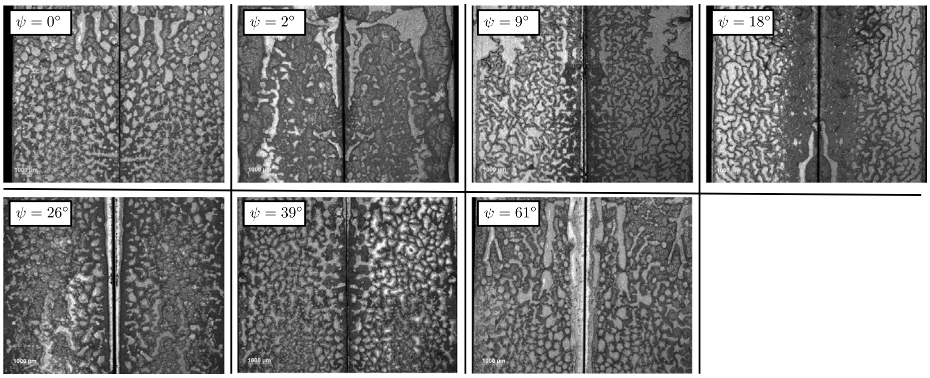

Fig. 14. Stereo light microscopy images of the top and bottom fracture surfaces of the delaminated samples $T = 250$ [$°C$] microflakes. The samples corresponding to mode angles $\psi = 0°$ and $\psi > 26°$ do not show a significant difference. The samples of mode angles $\psi = 2°$, $\psi = 9°$ and $\psi = 18°$ differ: the left fracture surface of the sample appears brighter, indicating the visibility of the BSM layer, thus suggesting interface failure.

range. Further differences could be due to the two different testing methods, ENF versus MMMB. The MMMB test measures the pure mode II toughness, whereas the ENF test measures the mode II toughness under additional out-of-plane compression which overestimates the real mode II toughness due to (additional) friction along the cracked interface, especially for porous materials (note that in the application out-ofplane compression is not present).

The microflake-based sintered silver measured in this work shows a comparable toughness, with $\Gamma_{I,C}$ of 10–17 [J/m^2] and $\Gamma_{II,C}$ of approximately 25 [J/m^2] at porosities of 30–26%. These results confirm the values reported in the literature, where lower porosity correlates with higher fracture toughness for mode I and mode II. Although the μF-sintered silver is on the lower side compared to the results of Dai et al. [55], who obtained a mode I fracture toughness of 36.9 [J/m^2], the μF sintered silver's layered microstructure

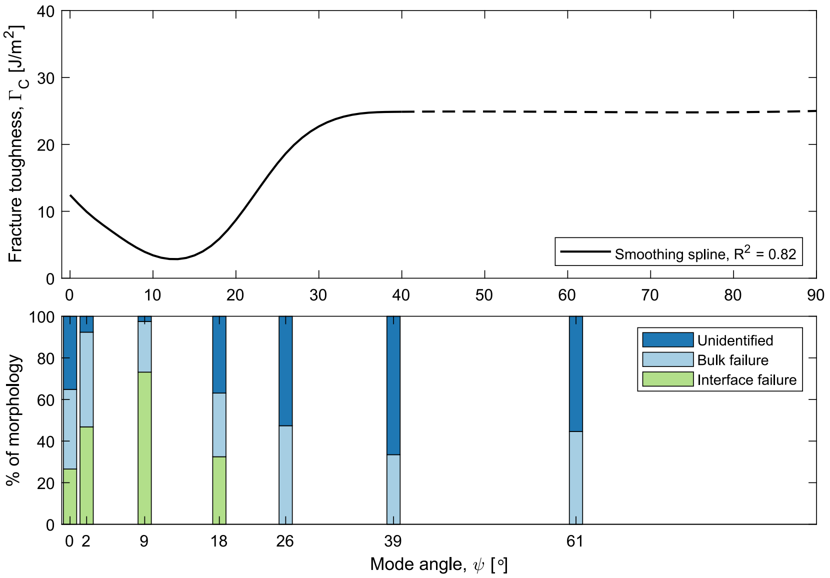

Fig. 15. The fracture toughness versus mode angle and the morphology distribution as a function of the mode angle obtained from the histogram images of Fig. 14. What can be seen is a maximum contribution in interface failure at the dip in fracture toughness.

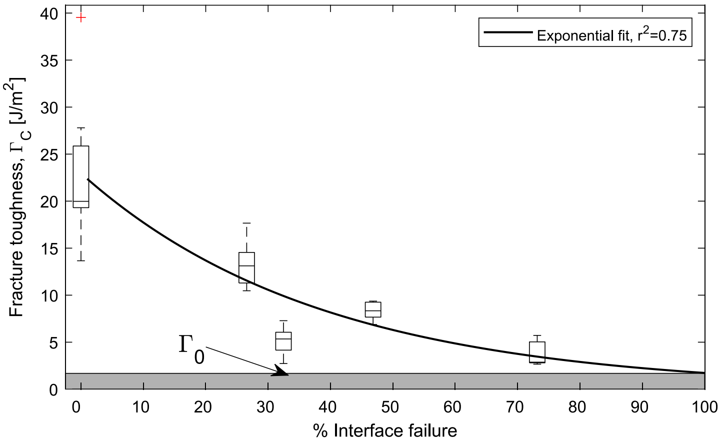

Fig. 16. The percentage of interface failure versus the fracture toughness data obtained from the sintered silver interconnect containing microflakes to estimate the thermodynamic work of adhesion Γ_0.

might play the biggest role in the difference between the two values.

4. Conclusion

Motivated by the increasing need for reliable interconnect materials, this study presents results of the interface fracture toughness of two different sintered silver materials, sintered at two temperatures. The experimental methods involved the sintering of two different sintered silver materials: one containing microflakes and one containing nanoparticles. The interconnect materials were sintered between two copper plates electroplated with a silver backside metallisation layer. These samples were used to provide microstructural images of the sintered silver interconnects obtained before and after fracture, and were tested using a dedicated mixed-mode delamination tester under in situ optical microscopy from which the fracture toughness was determined as a function of the mode mix from mode I to mode II. The following conclusions are drawn from the current research:

1. The mixed-mode fracture toughness of the NP-based sintered silver follows an approximately linear relationship as function of the mode angle. The sintering temperature does not influence the mixed-mode behaviour; only the magnitude is affected. This was explained by the improved small-scale homogeneity with increasing temperature as observed in the microstructural cross-sections. From the fractured samples, it was seen that the morphology remained consistent at various mode mixities.

Table 1
Literature results of the fracture toughness for sintered silver and the porosity, as reported in the references given in the right column. Note that the porosity range is reported from high-to-low, as these values related to the low-to-high range of the fracture toughness values. NiC tubes indicated a sintered silver reinforced with nickel-coated multiwall carbon nanotubes. The observed failure mechanism is bulk (B), interface (I) or a combination, mixed (M).* denoted extrapolated values from the mixed-mode fit.

Test	$\Gamma_{I,C}$ [J/m^2]	$\Gamma_{II,C}$ [J/m^2]	Porosity [%]	Failure	
Micro-cantilever beam	1.8–4.2			B	[56]
Dogbone test	7.68			B	[56]
3-pt chevron	0.08			I	[57]
Compact tension	0.074–0.226			I	[26]
ENF		5–330	34–24	I→B	[30]
ENF (bare Cu)		21–334	30 ± 3–25 ± 2	I	[25]
ENF (Ag-BSM)		277–969	30 ± 3–25 ± 2	M	[25]
ENF tests		41 ± 9–87 ± 22	33–29	I	[27]
DCB (virgin)	36.9		28	I	[55]
DCB (NiC tubes)	70.1		25	B	[55]
MMMB (NP)	35–115	600–800*	19–14	M	n.a.
MMMB (μF)	10–17	25*	30–26	M	n.a.

Consequently, the measured increase in fracture toughness is caused by the increase in plastic deformation around the crack tip in the interconnect.

2. The μF-based sintered silver displays a global minimum in fracture toughness between $0° < \psi < 38°$, followed by an almost flat dependence. Further examination uncovered that the fracture morphology changed with varying mode mixities. The samples in the range of $0° < \psi < 26°$ showed a preference for interface failure, whilst the remaining samples showed a preference for bulk failure. Samples close to the global minimum were shown to have the highest adhesive-to-cohesive ratio, up to 70% of the sample's surface. Subsequently, the thermodynamic work of adhesion was estimated to be around 1.7 [J/m^2]. Combined with the earlier conclusion that for the NP material, the fracture morphology remained consistent across the mode mixities, it was concluded that the peculiar mixed-mode fracture behaviour can be attributed to a change in the microscopic failure mechanism at low mode angles.
3. The fracture toughness values obtained in this study for both NP-based and μF-based sintered silver are in the same range as those reported in the literature, indicating consistency with previously obtained results despite differences in testing methods and material microstructures.

The findings of this study offer valuable insight into the complex interplay of sintering parameters, microstructure, and the resulting fracture behaviour around adhered interfaces, such as the sudden activation of an additional microscopic failure mechanism that depends on the mode angle. The clear dependence of fracture toughness on the mode angle and microstructure composition underlines the need for microstructural mechanical research to couple the sintered silver microstructure to the macroscopic behaviour.

CRediT authorship contribution statement

Noud P.T. Schoenmakers: Writing – original draft, Writing – review & editing, Methodology, Investigation, Formal analysis, Conceptualization. **Johan P.M. Hoefnagels:** Writing – review & editing, Supervision, Methodology, Conceptualization. **Edsger C.P. Smits:** Writing – review & editing, Supervision, Conceptualization. **Olaf van der Sluis:** Writing – review & editing, Supervision, Methodology, Conceptualization.

Declaration of competing interest

The authors declare the following financial interests/personal relationships which may be considered as potential competing interests: Noud P.T. Schoenmakers reports financial support was provided by Chip Integration Technology Center Foundation. If there are other authors, they declare that they have no known competing financial interests or personal relationships that could have appeared to influence the work reported in this paper.

Acknowledgements

The authors wish to thank Marc van Maris and Mark Vissers (Multiscale Lab TU/e) for their guidance and support in the experimental setup and Chip Integration Technology Center (CITC) and Henry A. Martin (CITC) for their support and providing samples.

Data availability

The data that has been used is confidential.

References

[1] Tummala RR, Rymaszewski EJ, Lee YC. Microelectronics packaging handbook, vol. 111, Springer-Science+Business Media, B.V.; 1989, http://dx.doi.org/10.1115/1.3226540.

[2] European Parliament. Directive 2000/53/EC of the European parliament and of the council of 18 2000 on end-of life vehicles. 2000.

[3] European Parliament. Restriction of hazardous substances in electrical and electronic equipment (RoHS). 2011.

[4] Wang J, Chen S, Zhang L, Zhao X, Duan F, Chen H. Brief Review of Nanosilver Sintering: Manufacturing and Reliability. J Electron Mater 2021;50(10):5483–98. http://dx.doi.org/10.1007/s11664-021-09078-1.

[5] Yang CA, Kao CR. Study of sintered nano-silver die attachment materials doped with indium. In: Proceedings - electronic components and technology conference 2016. 2016, p. 2468–74. http://dx.doi.org/10.1109/ECTC.2016.71.

[6] Gallagher C, Matijasevic G, Maguire J. Transient liquid phase sintering conductive adhesives as solder replacements. In: 1997 proceedings 47th electronic components and technology conference. IEEE; 1997, p. 554–60. http://dx.doi.org/10.1109/ECTC.1997.606223.

[7] German R. Sintering: from empirical observations to scientific principles. Elsevier; 2014, http://dx.doi.org/10.1016/C2012-0-00717-X, https://linkinghub.elsevier.com/retrieve/pii/C2012000717X.

[8] Morris JE, editor. Nanopackaging. Cham: Springer International Publishing; 2018, http://dx.doi.org/10.1007/978-3-319-90362-0.

[9] Li G, Fana J, Liao S, Zhua P, Zhang B, Zhao T, Sun R, Wong CP. Low temperature sintering of dendritic cu based pastes for power semiconductor device interconnection. In: Proceedings - electronic components and technology conference, vol. 2019-May, Institute of Electrical and Electronics Engineers Inc.; 2019, p. 81–6. http://dx.doi.org/10.1109/ECTC.2019.00020.

[10] Wang T, Chen X, Lu GQ, Lei GY. Low-temperature sintering with nano-silver paste in die-attached interconnection. J Electron Mater 2007;36(10):1333–40. http://dx.doi.org/10.1007/s11664-007-0230-5.

[11] Suganuma K, Sakamoto S, Kagami N, Wakuda D, Kim KS, Nogi M. Low-temperature low-pressure die attach with hybrid silver particle paste. Microelectron Reliab 2012;52(2):375–80. http://dx.doi.org/10.1016/j.microrel.2011.07.088.

[12] Le Henaff F, Azzopardi S, Deletage J, Woirgard E, Bontemps S, Joguet J. A preliminary study on the thermal and mechanical performances of sintered nano-scale silver die-attach technology depending on the substrate metallization. Microelectron Reliab 2012;52(9–10):2321–5. http://dx.doi.org/10.1016/j.microrel.2012.06.121.

[13] Siow KS. Are sintered silver joints ready for use as interconnect material in microelectronic packaging? J Electron Mater 2014;43(4):947–61. http://dx.doi.org/10.1007/s11664-013-2967-3.

[14] Seal S, Glover MD, Mantooth HA. Nanosilver preform assisted die attach for high temperature applications. In: Conference proceedings - IEEE applied power electronics conference and exposition. APEC 2015-May, 2015, p. 2925–30. http://dx.doi.org/10.1109/APEC.2015.7104766.

[15] Seal S, Glover MD, Alan Mantooth H. Application and reliability analysis of sintered silver preforms for die attachment of wide bandgap devices. In: WiPDA 2015-3rd IEEE workshop on wide bandgap power devices and applications. 2015, p. 377–82. http://dx.doi.org/10.1109/WiPDA.2015.7369326.

[16] Ang D. DA295A non-pressure sinter paste data sheet. Tech. rep., Heraeus; 2019.

[17] Tanaka Material R & D. Properties of hybrid sintering Ag adhesive; TS-9853. Tech. rep., Tanaka; 2019.

[18] Yu C, Yang D, Zhao D, Sheng Z. Reliability of nano-silver soldering paste with high thermal conductivity. In: 2019 20th international conference on electronic packaging technology. ICEPT 2019, 2019, http://dx.doi.org/10.1109/ICEPT47577.2019.9080930.

[19] Hong WS, Kim MS, Oh C, Joo Y, Kim Y, Hong K-K. Pressureless silver sintering of silicon-carbide power modules for electric vehicles. JOM 2020;72(2):889–97. http://dx.doi.org/10.1007/s11837-019-03815-y.

[20] Dai J, Li J, Agyakwa P, Corfield M, Johnson CM. Reliability and characterization of nanosilver joints prepared by a time-reduced sintering process. IEEE Trans Device Mater Reliab 2021;21(4):536–43. http://dx.doi.org/10.1109/TDMR.2021.3118323.

[21] Ordonez-Miranda J, Hermens M, Nikitin I, Kouznetsova VG, van der Sluis O, Ras MA, Reparaz J, Wagner M, Sledzinska M, Gomis-Bresco J, Sotomayor Torres C, Wunderle B, Volz S. Measurement and modeling of the effective thermal conductivity of sintered silver pastes. Int J Therm Sci 2016;108:185–94. http://dx.doi.org/10.1016/j.ijthermalsci.2016.05.014.

[22] Gillman A, Roelofs MJ, Matouš K, Kouznetsova VG, van der Sluis O, van Maris MP. Microstructure statistics–property relations of silver particle-based interconnects. Mater Des 2017;118:304–13. http://dx.doi.org/10.1016/j.matdes.2017.01.005.

[23] Chen C, Nagao S, Zhang H, Jiu J, Sugahara T, Suganuma K, Iwashige T, Sugiura K, Tsuruta K. Mechanical deformation of sintered porous Ag die attach at high temperature and its size effect for wide-bandgap power device design. J Electron Mater 2017;46(3):1576–86. http://dx.doi.org/10.1007/s11664-016-5200-3.

[24] Lee BS, Yoon JW. Die-attach for power devices using the Ag sintering process: Interfacial microstructure and mechanical strength. Met Mater Int 2017;23(5):958–63. http://dx.doi.org/10.1007/s12540-017-6908-1.

[25] Zhao S, Dai Y, Qin F, Li Y, An T, Gong Y. Effect of surface finish metallization layer on shearing fracture toughness of sintered silver bonded joints. Eng Fract Mech 2022;264(2021):108355. http://dx.doi.org/10.1016/j.engfracmech.2022.108355.

[26] Wang S, Kirchlechner C, Keer L, Dehm G, Yao Y. Interfacial fracture toughness of sintered hybrid silver interconnects. J Mater Sci 2020;55(7):2891–904. http://dx.doi.org/10.1007/s10853-019-04212-1.

[27] Dai Y, Zhao S, Qin F, An T, Gong Y, Chen P. Shear fracture resistance enhancement through micropatterning on copper substrate for sintered nano silver joints. Int J Adhes Adhes 2023;125. http://dx.doi.org/10.1016/j.ijadhadh.2023.103422.

[28] Van der Sluis O, Remmers JJ, Thurlings M, Welling B, Noijen SP. The competition between adhesive and cohesive fracture at amicro-patterned polymer-metal interface. Key Eng Mater 2013;577–578:225–8. http://dx.doi.org/10.4028/www.scientific.net/KEM.577-578.225.

[29] Li Y, Dai Y, Qin F, Zhao S. Loading rate on mode II fracture toughness of sintered silver. In: 2021 22nd international conference on electronic packaging technology. ICEPT 2021, Institute of Electrical and Electronics Engineers Inc.; 2021, p. 1–4. http://dx.doi.org/10.1109/ICEPT52650.2021.9568220.

[30] Zhao S, Dai Y, Qin F, Li Y, Liu L, Zan Z, An T, Chen P, Gong Y, Wang Y. On mode II fracture toughness of sintered silver based on end-notch flexure (ENF) test considering various sintering parameters. Mater Sci Eng A 2021;823:141729. http://dx.doi.org/10.1016/j.msea.2021.141729.

[31] Liu L, Shinozaki K. Fracture toughness enhancement via sub-micro silver-precipitation in silica glass fabricated by spark plasma sintering. J Am Ceram Soc 2022;105(3):1980–91. http://dx.doi.org/10.1111/jace.18214.

[32] Kang R, Dai Y, Qin F, Li Y. Thickness effect on shear fracture toughness of sintered silver joints. In: 2023 24th international conference on electronic packaging technology. ICEPT 2023, Institute of Electrical and Electronics Engineers Inc.; 2023, p. 1–5. http://dx.doi.org/10.1109/ICEPT59018.2023.10492034.

[33] Liu X, Dai Y, Kang R, Zhao L, Qin F. Determination of cohesive zone model (CZM) and numerical analysis of interface fracture in sintered silver with different metallization layers. In: 2024 25th international conference on electronic packaging technology. ICEPT, IEEE; 2024, p. 1–4. http://dx.doi.org/10.1109/ICEPT63120.2024.10668546.

[34] Kolluri M, Thissen MH, Hoefnagels JP, van Dommelen JA, Geers MG. In-situ characterization of interface delamination by a new miniature mixed mode bending setup. Int J Fract 2009;158(2):183–95. http://dx.doi.org/10.1007/s10704-009-9356-1.

[35] Kolluri M, Hoefnagels JP, Van Dommelen JA, Geers MG. An improved miniature mixed-mode delamination setup for in situ microscopic interface failure analyses. J Phys D: Appl Phys 2011;44(3). http://dx.doi.org/10.1088/0022-3727/44/3/034005.

[36] Neggers J, Hoefnagels JP, van der Sluis O, Sedaghat O, Geers MG. Analysis of the dissipative mechanisms in metal-elastomer interfaces. Eng Fract Mech 2015;149:412–24. http://dx.doi.org/10.1016/j.engfracmech.2015.06.056.

[37] Kolluri M, Hoefnagels JPM, Samimi M, van Dommelen H, van der Sluis O, Geers MGD. An in situ experimental-numerical approach for characterization and prediction of interface delamination: Application to CuLF-MCE systems. Adv Eng Mater 2012;14(11):1034–41. http://dx.doi.org/10.1002/adem.201200110.

[38] Gdoutos EE. Fracture mechanics – an introduction. 3rd ed. Springer International Publishing; 2020, http://dx.doi.org/10.1007/978-3-030-35098-7.

[39] Kolluri M, Hoefnagels JPM, van Dommelen J, Geers MGD. A practical approach for the separation of interfacial toughness and structural plasticity in a delamination growth experiment. Int J Fract 2012;183:1–18. http://dx.doi.org/10.1007/s10704-013-9871-y.

[40] Samimi M, van Dommelen JA, Kolluri M, Hoefnagels JP, Geers MG. Simulation of interlaminar damage in mixed-mode bending tests using large deformation self-adaptive cohesive zones. Eng Fract Mech 2013;109:387–402. http://dx.doi.org/10.1016/j.engfracmech.2012.09.017.

[41] Barsoum RS. Application of quadratic isoparametric finite elements in linear fracture mechanics. Int J Fract 1974;10(4):603–5. http://dx.doi.org/10.1007/BF00155266.

[42] Barsoum RS. Further application of quadratic isoparametric finite elements to linear fracture mechanics of plate bending and general shells. Int J Fract 1975;11(1):167–9. http://dx.doi.org/10.1007/BF00034724.

[43] Van der Sluis O, Vossen B, Neggers J, Ruybalid A, Chockalingam K, Peerlings R, Hoefnagels J, Remmers J, Kouznetsova V, Schreurs P, Geers M. Advances in delamination modeling of metal/polymer systems: Continuum aspects. In: Nanopackaging: nanotechnologies and electronics packaging. 2nd ed. Springer International Publishing; 2018, p. 83–128. http://dx.doi.org/10.1007/978-3-319-90362-0{_}3.

[44] Wei L, Edwards L, Fitzpatrick M. FE analysis of stresses and stress intensity factors of interfacial cracks in a CTS specimen. Eng Fract Mech 2002;69(1):85–90. http://dx.doi.org/10.1016/S0013-7944(01)00072-8.

[45] Choupani N. Characterization of fracture in adhesively bonded double-lap joints. Int J Adhes Adhes 2009;29(8):761–73. http://dx.doi.org/10.1016/j.ijadhadh.2009.05.002.

[46] Yu H, Kuna M. Interaction integral method for computation of crack parameters K–T – A review. Eng Fract Mech 2021;249. http://dx.doi.org/10.1016/j.engfracmech.2021.107722.

[47] Chan S, Tuba I, Wilson W. On the finite element method in linear fracture mechanics. Eng Fract Mech 1970;2(1):1–17. http://dx.doi.org/10.1016/0013-7944(70)90026-3.

[48] Xuan ZC, Khoo BC, Li ZR. Computing bounds to mixed-mode stress intensity factors in elasticity. Arch Appl Mech 2006;75(4–5):193–209. http://dx.doi.org/10.1007/s00419-005-0388-3.

[49] O'Haver T. A pragmatic introduction to signal processing applications in scientific measurement. 2024, URL https://terpconnect.umd.edu/~toh/spectrum/TOC.html.

[50] Chockalingam K, Kouznetsova V, van der Sluis O, Geers M. 2D phase field modeling of sintering of silver nanoparticles. Comput Methods Appl Mech Engrg 2016;312:492–508. http://dx.doi.org/10.1016/j.cma.2016.07.002, phase Field Approaches to Fracture.

[51] Knoer M, Schletz A. Power semiconductor joining through sintering of silver nanoparticles: Evaluation of influence of parameters time, temperature and pressure on density, strength and reliability. In: 6th international conference on integrated power electronics systems. CIPS, IEEE; 2010, p. 1–6, URL https://ieeexplore.ieee.org/document/5730660/citations?tabFilter=papers#citations.

[52] Hutchinson JW, Suo Z. Mixed mode cracking in layered materials. Adv Appl Mech 1991;29(C):63–191. http://dx.doi.org/10.1016/S0065-2156(08)70164-9.

[53] Volinsky A, Moody N, Gerberich W. Interfacial toughness measurements for thin films on substrates. Acta Mater 2002;50(3):441–66. http://dx.doi.org/10.1016/S1359-6454(01)00354-8.

[54] de Moura MF, de Morais AB. Equivalent crack based analyses of ENF and ELS tests. Eng Fract Mech 2008;75(9):2584–96. http://dx.doi.org/10.1016/j.engfracmech.2007.03.005.

[55] Dai Y, Zhao L, Zan Z, Qin F. Mode I fracture of sintered nano-silver doped with nickel-coated multiwall carbon nanotube. Mater Sci Semicond Process 2024;174:108171. http://dx.doi.org/10.1016/j.mssp.2024.108171.

[56] Chen C, Nagao S, Suganuma K, Jiu J, Sugahara T, Zhang H, Iwashige T, Sugiura K, Tsuruta K. Macroscale and microscale fracture toughness of microporous sintered Ag for applications in power electronic devices. Acta Mater 2017;129:41–51. http://dx.doi.org/10.1016/j.actamat.2017.02.065.

[57] Wereszczak AA, Modugno MC, Chen BR, Oistad BA. Apparent fracture toughness of pressureless sintered silver interconnects. Tech. Rep., Oak Ridge: Oak Ridge National Laboratory; 2018, http://dx.doi.org/10.2172/1456805.